Preprints (www.preprints.org) | NOT PEER-REVIEWED | Posted: 22 April 2020 doi:10.20944/preprints202003.0355.v2

Soft Sensing Based In Situ Control of Thermo-Fluidic Processes in DoD Inkjet Printing

Amritam Das*[1], Martijn Princen[1], Mahnaz Shokpour Roudbari[2], Amol Khalate[2], Siep Weiland[1]

***Abstract*—This paper introduces a closed-loop control strategy for maintaining consistency of liquid temperature in commercial Drop on Demand (DoD) inkjet printing. No additional sensors or additional actuators are installed in the printhead while achieving the consistency in liquid temperature. To this end, this paper presents a novel in situ sensing-actuation policy at every individual liquid-nozzle, where the jetting mechanism has three distinct roles. It is used for jetting liquid droplet onto the print media based on the print-job. It is used as a soft sensor to estimate the real-time liquid temperature of the jetting nozzle. While not jetting liquid, it is used as a heating actuator to minimize the gradient of liquid temperature among nozzles. The soft sensing based in situ controller is implemented in an experimentally validated digital twin that models the thermo-fluidic processes of the printhead. The digital twin is scalable and flexible to incorporate an arbitrary number of liquid-nozzles, making the control strategy applicable for future designs of the printhead.**

***Index Terms*—Inkjet Printing, Thermo-Fluidic Processes, Spatially Interconnected Systems, Soft Sensing, Optimal Control.**

I. INTRODUCTION

Printing makes the human intellect tangible and timeless. From the early Gutenberg Press in the fifteenth century until today's printing technology, the documentation in print has enabled humanity to preserve its creativity in the form of books, crafts, and numerous consumable objects. Until the nineteenth century, human operators were employed to execute printing jobs manually using press machines [1]. During the early 1950s, the introduction of digital computers loomed the possibility of printing digital images on a medium without human intervention. The printing press was substituted by the digital inkjet technology in which liquid droplets are deposited on a solid medium to replicate digital images in an automated fashion [2]. Since then, inkjet-based digital printing has been improved to be a faster, more cost-effective, and energy-efficient process. The non-contact and additive nature of inkjet printing has also attracted versatile applications. With the emergence of additive micro-manufacturing, inkjet printing is now applicable to a wide range of materials, including polymers and metals, and also various media like textile, wood, and circuit boards [3]. Thanks to the technical developments in inkjet-based digital printing, we are now gradually transcending 'from the world of paper printing to printing the world.'

Today, the printer is a commercial peripheral which produces printed products based on the user's demand. Due to the constant increase in the market competition of inkjet printing, the print quality stands out to be a decisive factor. In general, the print quality indicates how accurate the printed product resembles its digital counterpart. However, the quantitative metric which determines the quality of the printed product depends mainly on the application area and the user group. For example, in paper printing, the measure of quality is typically determined by the reflectance of the printed area, print density variations, offsets of the printed pixels, etc. [4]. For textile printing, the measure of quality is the gloss of the printed surface, texture geometry, surface smoothness of the printed area, etc. [3].

As the application domain of inkjet printing is quite diverse, printer manufacturers concentrate on how to improve the general process of inkjet printing instead of considering any application-specific metric. To this end, the primary motivation behind this research is to enhance the role of liquid droplets on improving the print quality irrespective of the printing medium and its application. One can view the inkjet printing process as a physical integration of liquid droplets with a solid medium. This process is also known as *jetting*. Based on the user-defined print-job (a set of to-be-printed images), the jetting process deposits droplets of liquid on a solid medium (e.g., a sheet of paper). A set of printheads is responsible for generating and jetting the droplets in the right sequence, at the right position, with a pre-specified volume and with well-defined (or carefully controlled) physio-chemical properties.

A. Drop on Demand (DoD) Inkjet Printhead

A Drop on Demand (DoD) inkjet printhead jets droplets of liquid based on the specific image that the user demands to print. A typical architecture of a commercial DoD printhead is shown in Figure 1a (for instance, see XAAR printhead [5]). Here, the bottom stage of the printhead is called the nozzle-platform (NP), which is divided into two mutually insulated parts NP_{left} and NP_{right}. Each part of NP consists of an array (divided into rows and columns) of nozzles. An example of the nozzles' placement with respect to an NP is shown in Figure 1b. The NP can be removed from the printhead and replaced with a new design. This feature allows for accommodating arbitrary numbers of nozzles without re-designing the entire printhead. On arrival of a print-job, the following aspects play key roles in the jetting process:

[1]Eindhoven University of Technology, Department of Electrical Engineering, Control Systems group, P.O. Box 513, 5600 MB Eindhoven, The Netherlands. E-mail: amritamabroad@gmail.com, M_princen@hotmail.com, s.weiland@tue.nl

[2]Canon Production Printing B.V., Van der Grintenstraat 10, 5914 HH Venlo, The Netherlands. E-mail: mahnaz.shokrpour@cpp.canon, amolkhalate@gmail.com

*Corresponding author: Amritam Das. Tel. +31(0)402472300.

© 2020 by the author(s). Distributed under a Creative Commons CC BY license.

Preprints (www.preprints.org) | NOT PEER-REVIEWED | Posted: 22 April 2020 doi:10.20944/preprints202003.0355.v2

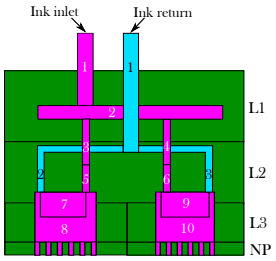

(a) Cross-sectional view of a printhead.

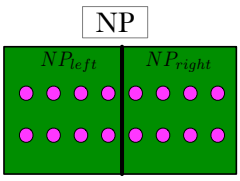

(b) Bottom-view of an NP with nozzles.

Fig. 1: The printhead consists of solid components (green), and channels for liquid (inlet in purple and return in blue).

1) DoD Bit-map: The user-defined image is translated into a bit-map. A bit-map stores the sequence in which nozzles are used for drop formation.

2) Liquid Inlet and Liquid Re-Circulation: Based on the image, the required flow rate for the deposition and re-circulation of liquid is pre-determined and assigned for every individual nozzle.

3) Mechanism for DoD Drop Formation: Every individual nozzle comprises a conduit, a liquid chamber, and a mechanism for ejecting liquid from the chamber, through the conduit, onto a printing media. This jetting mechanism is equipped with a piezoelectric element attached to a diaphragm. Depending on a specific bit-map, a voltage pulse is applied to the piezoelectric element using a drive circuit. Actuation of the piezoelectric element forms a pressure wave inside the nozzle to create a droplet of liquid with pre-defined volume and push it out onto the medium. The frequency at which the jetting mechanism is actuated is in the range of kilo-Hertz [4](pp. 9-10).

B. Quality Limiting Aspects in DoD Inkjet Printhead

In DoD inkjet printing, print quality depends on the physio-chemical properties of every individual droplet (these properties are viscosity, surface tension, temperature, and the speed of sound inside the nozzle). During printing, these properties of droplets may deviate from their desired values. As a consequence, the pre-defined actuation pulse does not jet the droplet of desired physio-chemical qualities, and, therefore, results in poor print quality.

Two factors play crucial roles behind the deterioration of the droplet properties: a) nozzles acoustics, and b) the temperature of liquid droplets. In [6], the problems related to nozzle acoustics are solved using a feedforward controller. The current paper considers that adequate measures are already incorporated to take into account the problems related to nozzle acoustics and, hence, will not be discussed. On the other hand, during the jetting process, temperature fluctuation of liquid droplets among the nozzles is an unresolved problem that severely affects the print quality. Temperature fluctuation may occur due to the following reasons:

1) Heat Dissipation in Nozzles: During jetting piezoelectric element dissipates heat [4] (page 2). Moreover, depending on drop volume, a jetting droplet results in impeding thermal energy. In particular, if not all the nozzles in the NP are simultaneously used for jetting, a gradient in liquid temperature among jetting and non-jetting nozzles is a serious problem [7] (page 477).

2) Thermal Cross-talk in Solid and Liquid: In Figure 1b, the array of nozzles are physically coupled via the solid structure of the NP. Due to the different physical properties of solid and liquid, their mutual cross-talk causes changes in temperature among nozzles as well as adjacent printheads.

The exchange of thermal energy (heat flux) on mutually interacting solid and liquid substances is a *thermo-fluidic process*. Concerning inkjet printing, the effect of this thermo-fluidic process is the temperature fluctuation of liquid droplets among nozzles, and poor print quality is the immediate consequence.

C. Contribution

In the printing industry, model-based control of thermo-fluidic aspects is an unexplored field of research. Most of the literature is on physical modeling and experimental methods of drop formation and relevant fluid dynamics in inkjet printing (c.f. [2], [8], [9]). The applications of control techniques are largely restricted to designing the DoD voltage pulses for generating droplets and compensating problems related to nozzle acoustics (c.f. [4], [6], [10]). In general, a system-theoretic outlook to model and control thermo-fluidic aspects in DoD inkjet printing is still mostly missing.

This paper introduces, for the first time, a model-based feedback controller for the DoD inkjet printhead that uses no additional sensors and no additional actuators to compensate for the fluctuation of liquid temperature among nozzles. The applicability of the control system is demonstrated with the help of three novel contributing aspects:

1) The modeling framework presents a digital twin of the printhead, which is modular towards an arbitrary number of nozzles. Changes in the number of nozzles do not require redevelopment of the digital twin from the outset.
2) The piezoelectric elements that are already installed in every individual nozzle are used as collocated soft sensors. The self-sensing capability of a piezoelectric element is exploited to develop a data-driven algorithm and estimate the liquid temperature at every individual nozzle.
3) A concept of in situ actuation is introduced to control the fluctuation of liquid temperature. Here, a sensing-

Preprints (www.preprints.org) | NOT PEER-REVIEWED | Posted: 22 April 2020 doi:10.20944/preprints202003.0355.v2

actuation policy is developed such that the controller uses the bit-map to anticipate the change in temperature at every nozzle and utilizes only the non-jetting nozzles to compensate for the temperature fluctuation.

D. Organization of The Paper

The remainder of this paper is organized as follows. After a brief explanation of the notations in Section II, a graph-theoretic modeling framework is presented in Section III to design the digital twin. In Section IV, the piezoelectric element is used as a soft sensor to estimate the liquid temperature at every individual nozzle. In Section V, the developed digital twin and the soft sensor are validated using an experimental set-up. A model predictive controller for compensating the fluctuation of liquid temperature is developed and demonstrated in Section VI. Section VII provides some concluding remarks.

II. NOTATIONS

A set of natural numbers is denoted by $\mathbb{N}$. Given two positive integers $0 < n < m$, the subset $\mathbb{N}_{[n,m]} := \{n, n+1, \cdots, m\} \subset \mathbb{N}$ denotes all natural number between n and m including n, m. The set of $n \times n$ positive semi-definite and positive definite matrices are denoted by $\mathbb{S}^n_{\succcurlyeq 0}$ and $\mathbb{S}^n_{\succ 0}$, respectively. Let a be a complex number defined as $a := x+jy$ with $j = \sqrt{-1}$. Then, $\mathrm{Re}(a)$ denotes the real-part of a, i.e. x and $\mathrm{Im}(a)$ denotes the imaginary-part of a, i.e. jy. The complex conjugate of a is defined by $a^* = x - jy$. Hermitian transpose of a $m \times n$ complex-valued matrix A is denoted by A^{H}. For a matrix $A \in \mathbb{R}^{m \times n}$, $A^\dagger$ denotes the pseudo-inverse of A.

Remark II.1. Due to confidentiality reasons, in this paper, all the plots are normalized by subtracting the data points with a fixed nominal value.

III. A DIGITAL TWIN OF THERMO-FLUIDIC PROCESSES: PHYSICAL MODELING

The first objective of the paper is to develop a digital twin of the jetting process for describing its thermo-fluidic aspects. The digital twin constitutes a generic physical model of the thermo-fluidic processes that can be used throughout the design cycle. The digital twin must meet the following properties:

1) *Modularity:* The model is modular with respect to an arbitrary number of nozzles.
2) *Flexibility:* The model is flexible such that, during any stage of prototyping, necessary adaptation and modification on the model can be easily incorporated.
3) *Versatility:* The model serves as a versatile tool that can be used for simulation, design optimization, fault diagnosis, control design and experimental validation.

To cope with the ever-increasing demands on throughput, the modularity of the digital twin offers the freedom of increasing the number of nozzles without the need of re-modeling. A flexible modeling approach can easily incorporate necessary adaptation at different stages of the design cycle, especially during experimental validation with increasing accuracy, and with supplementing additional functionality.

A. A Graph-Theoretic Modeling Framework

This paper presents a graph-theoretic framework that makes the digital twin modular, flexible and versatile. The graph-theoretic model consists of the following three definitions:

D.1 *Topology*: A finite and connected graph consists of a set of nodes $\mathcal{N}$ and edges $\mathcal{E}$. It is defined by the following triad

$$\mathcal{G} = (\mathcal{N},\ \mathcal{E},\ \mathbb{T}). \tag{1}$$

- The time axis is defined by set $\mathbb{T}$. If the thermo-fluidic processes are modeled in continuous time, $\mathbb{T} := [0, \infty)$. If discrete time is considered to model the thermo-fluidic processes, $\mathbb{T} := \{kt_d \mid k \in \mathbb{N} \cup \{0\}\}$, where the sampling period t_d is a fixed scalar. The time index is denoted by $t \in \mathbb{T}$.
- Each object $\mathcal{N}_i$ in the set $\mathcal{N}$, $i \in \mathbb{N}_{[1,m]}$, is a node or component of the graph.
- The set of edges $\mathcal{E} = \{\mathcal{E}_{i,j} \mid \text{for all } (i,j) \text{ with } A_{i,j} = 1\}$ describes the interconnection between a particular node and its neighbourhood nodes. Here, $A \in \mathbb{N}^{m \times m}$ is an adjacency matrix that has either zero or one as its elements depending on whether the nodes $\mathcal{N}_i$ and $\mathcal{N}_j$ are physically attached or not. Precisely, its entries

$$A_{i,j} = \begin{cases} 1, & \text{if } \mathcal{N}_i \text{ is connected to } \mathcal{N}_j \\ 0, & \text{otherwise.} \end{cases}$$

D.2 *Edges*: Every individual edge $\mathcal{E}_{i,j} \in \mathcal{E}$ is defined by the following couple:

$$\mathcal{E}_{i,j} = (\mathcal{L}^I_{i,j}, \mathcal{M}_{i,j}). \tag{2}$$

- Wherever $\mathcal{N}_i$ is interconnected to $\mathcal{N}_j$, i.e. $A_{i,j} = 1$, there are time-varying interconnection signals associated with the edge. Let these signals be $(l_{i,j}, l_{j,i}) : \mathbb{T} \to \mathcal{L}^I_{i,j}$, respectively.
- The relation among interconnection signals $l_{i,j}$ and $l_{j,i}$ defines a subspace $\mathcal{M}_{i,j} \subset \mathcal{L}^I_{i,j}$.

D.3 *Nodes*: Every individual node $\mathcal{N}_i$ is associated with the following triple:

$$\mathcal{N}_i = (\mathcal{S}_i, \mathcal{B}_i, \mathcal{P}_i). \tag{3}$$

- There are three categories of time-varying signals that belongs to a subspace $\mathcal{S}_i$ associated with every individual $\mathcal{N}_i$.
  (a) The internal state variable $x_i : \mathbb{T} \to \mathcal{X}_i$
  (b) The to-be-manipulated control signals $c_i : \mathbb{T} \to \mathcal{C}_i$.
  (c) Associated with every individual node, the collection of all interconnection signals is $l_i : \mathbb{T} \to \mathcal{L}_i$. They are related to an individual edge such that $\mathcal{L}^I_{i,j} \subseteq \mathcal{L}_i \times \mathcal{L}_j$.
  (d) The user-defined print-job introduces a set of signals that affect the node behaviour. They are given by $d_i : \mathbb{T} \to \mathcal{D}_i$.

  As a result, $\mathcal{S}_i := \mathcal{X}_i \times \mathcal{C}_i \times \mathcal{L}_i \times \mathcal{D}_i$.
- Print-job signals d_i always depend on the user-defined image that is captured in a bit-map. Given a specific bit-map, the signals d_i are restricted by a subspace $\mathcal{B}_i \subset \mathcal{D}_i$.

Preprints (www.preprints.org) | NOT PEER-REVIEWED | Posted: 22 April 2020 doi:10.20944/preprints202003.0355.v2

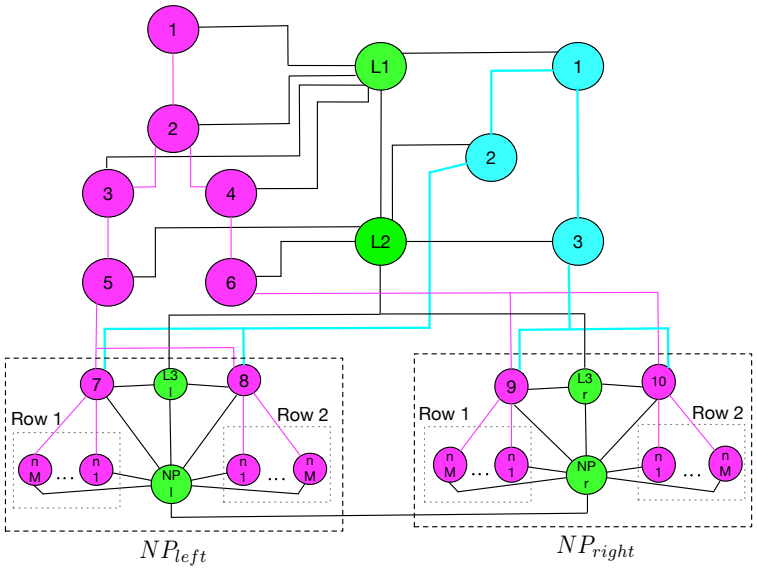

Fig. 2: Topology of the printhead with 4M nozzles (denoted by $n1, \cdots, nM$). ● represents a solid component, ● represents a liquid component for inlet, and ● represents a liquid component for re-circulation. ▬ is an edge describing conductive exchange of thermal energy between two solid components or a solid and liquid component. ▬ is an edge describing convective thermal energy due to the inflow of liquid along the inlet channels. ▬ is an edge describing convective thermal energy due to the re-circulation of liquid along the return channels.

- The behaviour of $\mathcal{N}_i$ is captured by a relation among all the signals (x_i, c_i, l_i, d_i) and defines a subspace $\mathcal{P}_i \subset \mathcal{S}_i$.

B. Graph-Theoretic Digital Twin for Thermo-Fluidic Processes

To implement a digital twin of the DoD inkjet printhead, the user simply requires to provide concrete specifications for each of the definitions (D.1)-(D.3). These specifications are given in the following items:

1) Printhead Topology: The digital twin of the printhead is a finite and connected graph according to the definition (D.1).

- Each node represents a solid or liquid component. For a specific design, the user specifies the number of nodes.
- The adjacency matrix A is defined based on the architecture of the printhead.
- Except for the adjustable NPs, the remaining architecture of the printhead is typically kept identical. Then, specifying the arrays of nozzles is sufficient for defining the entire topology of a newly designed printhead.
- The user defines $\mathbb{T}$ to specify whether the signals are in continuous time or discrete time.

For the printhead shown in figure 1a, individual nodes (components) and the interconnection topology, is depicted in figure 2.

2) Interconnection Among Components: The interconnection describes the exchange of thermal energy among adjacent components. The energy exchange is either conductive (between two solid components) or convective (between a solid and liquid component or between two liquid components). Typically, a bidirectional exchange of thermal energy occurs between two solid or a solid and a liquid component. A unidirectional exchange of thermal energy occurs between two adjacent liquid channels towards the direction of the flow. Hence, a distinction is made between an edge $\mathcal{E}_{i,j}$ and another edge $\mathcal{E}_{j,i}$ to distinguish between bidirectional and unidirectional interconnections.

To model an individual edge between adjacent components $\mathcal{N}_i$ and $\mathcal{N}_j$, i.e. wherever $A_{i,j} = 1$, the user must specify the following items according to (D.2):

- In terms of temperature of the adjacent nodes (°C), the interconnection signals between $\mathcal{N}_i$ and $\mathcal{N}_j$ are categorised into inputs $v_{i,j}(t) \in \mathbb{R}^{n_v^{ij}}$ and outputs $w_{i,j}(t) \in \mathbb{R}^{n_w^{ij}}$. Here, the user specifies the dimension of the interconnection signal $l_{i,j}(t)$, where $l_{i,j} := \text{col}(v_{i,j}, w_{i,j})$.
- Based on the conductive or convective thermal energy exchange, point-wise in time, the subspace $\mathcal{M}_{i,j}$ defines either uni-direction or bi-direction interconnection relations according to

$$\mathcal{M}_{i,j} := \{(l_{i,j}, l_{j,i}) \mid v_{j,i} = M_{i,j} w_{i,j} \wedge A_{i,j} = 1\}. \quad (4)$$

Wherever $A_{i,j} = 1$, the user specifies the relation (4) by defining a constant matrix $M_{i,j}$ of suitable dimension.

3) Solid or Liquid Components: For individual nodes, based on the physical properties and dimensions, the Biot number [11]–[13] justifies the possibility to consider a lumped model (finite dimensional) while neglecting the spatial variation of thermo-fluidic aspects in the component. A lumped model describes the evolution of temperature at individual node due to a) the conduction between two solid components, b) convection between two liquid components, c) convection between a solid and a liquid component.

To model an individual node $\mathcal{N}_i$, the user must specify the following items according to (D.3):

Preprints (www.preprints.org) | NOT PEER-REVIEWED | Posted: 22 April 2020 doi:10.20944/preprints202003.0355.v2

- The user specifies the dimension of the internal state variable $x_i(t) \in \mathbb{R}^{n_x^i}$ of individual node $\mathcal{N}_i$. In this case, x_i is the temperature (°C) of the solid or liquid component.
- Control signals are categorised into control inputs (in terms of thermal power (Watt) that can be manipulated) $u_i(t) \in \mathbb{R}^{n_u^i}$ and measured outputs (in terms of temperature (°C) that can be measured) $y_i(t) \in \mathbb{R}^{n_y^i}$. They define the control signals $c_i := \text{col}(u_i, y_i)$.
- Grouping together all the edges corresponding to an individual node, interconnection inputs $v_i(t) \in \mathbb{R}^{n_v^i}$ and outputs $w_i(t) \in \mathbb{R}^{n_w^i}$ are obtained. Based on the user-defined relation (4), these signals are constructed according to $v_i := \text{col}(v_{i,k})_{k\in\mathbb{I}_{i,j}}$ and $w_i := \text{col}(w_{i,k})_{k\in\mathbb{I}_{i,j}}$ with $\mathbb{I}_{i,j} = \{j | A_{i,j} = 1\}$. They define the interconnection signals $l_i := \text{col}(v_i, w_i)$ for an individual node $\mathcal{N}_i$.
- Using an user-defined bit-map, the flow parameters of inlet liquid and liquid return (m^3/sec) are known and stored in a time-varying matrix $\Theta(t)$ for all liquid channels. To allocate flow parameters for every individual node, an operator $\mathcal{T}_i$ is defined such that $\Theta_i(t) = (\mathcal{T}_i(\Theta))(t)$, where $\Theta_i(t)$ is the allocated flow parameter for the node $\mathcal{N}_i$.
  The function $\Theta_i(t)$ relates print-job associated inputs (in terms of convective heat flux, Watt) $p_i(t) \in \mathbb{R}^{n_p^i}$ and outputs $q_i(t) \in \mathbb{R}^{n_q^i}$ (in terms of thermal energy over unit volume of liquid, Kg°C/m^3) according to the following algebraic relation point-wise in time:
$$\mathcal{B}_i := \{d_i = \text{col}(p_i, q_i) \mid p_i = \Theta_i q_i\}. \tag{5}$$
  Here, (5) describes convective thermal energy transfer due to the change in the liquid flow of inlet and return for every individual node. Using user-defined $\Theta(t)$ and $\mathcal{T}_i$ in (5), the signals $d_i(t)$ and the matrix $\Theta_i(t)$ are automatically defined for individual node.
- The dynamic relations among defined signals (x_i, c_i, l_i, d_i) have the following input-state-output form:
$$\begin{bmatrix} Q_t(x_i)(t) \\ w_i(t) \\ q_i(t) \\ y_i(t) \end{bmatrix} = \begin{bmatrix} A^i_{xx} & B^i_{xv} & B^i_{xp} & B^i_{xu} \\ C^i_{wx} & D^i_{wv} & D^i_{wp} & D^i_{wu} \\ C^i_{qx} & D^i_{qv} & D^i_{qp} & D^i_{qu} \\ C^i_{yx} & D^i_{yv} & D^i_{yp} & D^i_{yu} \end{bmatrix} \begin{bmatrix} x_i(t) \\ v_i(t) \\ p_i(t) \\ u_i(t) \end{bmatrix} + \begin{bmatrix} f^i_x(t) \\ g^i_w(t) \\ g^i_q(t) \\ g^i_y(t) \end{bmatrix}. \tag{6}$$
  Equation (6) is derived using the laws of mass and energy balance (c.f. [14]). Based on the user's choice of $\mathbb{T}$, (6) can be used in either continuous time or discrete time. Accordingly, on functions $f : \mathbb{T} \to \mathbb{R}^n$, the operator Q_t is defined as
$$(Q_t(f))(t) := \begin{cases} \frac{\mathrm{d}f(t)}{\mathrm{d}t}, & \text{if } t \in \mathbb{R}^+, \\ f(t + t_d), & \text{if } t \in \{kt_d \mid k \in \mathbb{N} \cup \{0\}\}. \end{cases}$$
  Consequently, the definitions of constant matrices A^i_{xx}, B^i_{xv}, B^i_{xp}, B^i_{xu}, and the function f^i_x differ depending on the choice of $\mathbb{T}$.
  Based on the material properties, the chemical composition of the liquid and physical dimension of individual component in the printhead, the matrices A^i_{xx}, B^i_{xv}, B^i_{xp}, and B^i_{xu} are determined from the balance equations. They are real-valued constant matrices with suitable dimensions. The constant matrices $C^i_{m,n}$ and $D^i_{m,n}$ for $m, n \in \{x, v, w, p, q, u, y\}$ are suitably defined based on the topology, the availability of sensors and control actuators. The functions f^i_{cx}, g^i_w, g^i_q, g^i_y of suitable dimensions are introduced to model disturbances related to ambient temperature, convective losses due to movement of the carriage during printing, heating of the electronics etc.

Illustrative Example III.1. An example of building the thermo-fluidic model is given in the supplementary material.

C. Equivalent Classes of Thermo-Fluidic Model

In the previous exposition, the graph-theoretic representation (D.1)-(D.3) presents a paradigm for building and upscaling the thermo-fluidic model for a DoD printhead with arbitrary number of nozzles. Subsequently, a compact multi-input and multi-output (MIMO) representation may appear to be useful for design optimization or synthesizing an observer-based controller. By rearranging signals and performing algebraic operations, there are three ways to equivalent represent the graph theoretic model.

1) By Stacking Node Signals:

$$\bar{\mathcal{P}}_{\text{I}} := \left\{ \begin{array}{c} (x, c, l, d) \text{ such that,} \\ l \in \{l | v = \bar{M} w\}, \\ d \in \{d | p = \bar{\Theta} q\}, \\ \begin{bmatrix} Q_t(x) \\ w \\ q \\ y \end{bmatrix} = \begin{bmatrix} A_{xx} & B_{xv} & B_{xp} & B_{xu} \\ C_{wx} & D_{wv} & D_{wp} & D_{wu} \\ C_{qx} & D_{qv} & D_{qp} & D_{qu} \\ C_{yx} & D_{yv} & D_{yp} & D_{yu} \end{bmatrix} \begin{bmatrix} x \\ v \\ p \\ u \end{bmatrix} + \begin{bmatrix} f_x \\ g_w \\ g_q \\ g_y \end{bmatrix} \end{array} \right\}. \tag{7}$$

2) By Eliminating Interconnection Signals:

$$\bar{\mathcal{P}}_{\text{II}} := \left\{ \begin{array}{c} (x, c, d) \text{ such that,} \\ d \in \{d | p = \bar{\Theta} q\}, \\ \begin{bmatrix} Q_t(x) \\ q \\ y \end{bmatrix} = \begin{bmatrix} A & B_1 & B_2 \\ C_1 & D_{11} & D_{12} \\ C_2 & D_{21} & D_{22} \end{bmatrix} \begin{bmatrix} x \\ p \\ u \end{bmatrix} + \begin{bmatrix} f \\ g_1 \\ g_2 \end{bmatrix} \end{array} \right\}. \tag{8}$$

3) By Eliminating Print-Job Signals:

$$\bar{\mathcal{P}}_{\text{III}} := \left\{ \begin{array}{c} (x, c) \text{ such that,} \\ \begin{bmatrix} Q_t(x) \\ y \end{bmatrix} = \begin{bmatrix} \tilde{A} & \tilde{B} \\ \tilde{C} & \tilde{D} \end{bmatrix} \begin{bmatrix} x \\ u \end{bmatrix} + \begin{bmatrix} G \\ J \end{bmatrix} \end{array} \right\}. \tag{9}$$

All four representations of the thermo-fluidic model are depicted in figure 3. Among them, behaviour of the graph theoretic model (D.1)-(D.3) is equivalently described by $\bar{\mathcal{P}}_{\text{I}}$ in (7). The equivalence holds as (7) is a result of signal re-arrangement in (D.1)-(D.3). In particular, (x, c, l, d) are obtained by stacking the signals (x_i, c_i, l_i, d_i) in a column

Preprints (www.preprints.org) | NOT PEER-REVIEWED | Posted: 22 April 2020 doi:10.20944/preprints202003.0355.v2

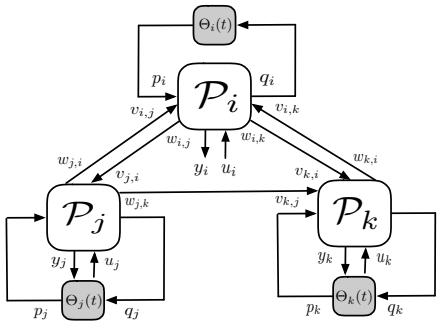

(a) Graph theoretic representation as defined by (D.1)-(D.3).

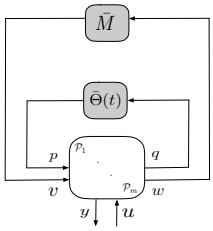

(b) Representation of $\bar{\mathcal{P}}_{\text{I}}$ in (7)

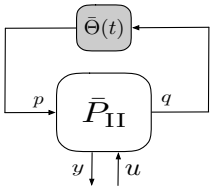

(c) Representation of $\bar{\mathcal{P}}_{\text{II}}$ in (8)

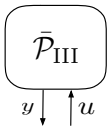

(d) Representation of $\bar{\mathcal{P}}_{\text{III}}$ in (9)

Fig. 3: Four equivalent representations of the thermo-fluidic model in the printhead.

for all $i \in \mathbb{N}_{[1,m]}$. In (7), the matrix $\bar{M}$ is constructed by combining the relation $v_{j,i} = M_{i,j} w_{i,j}$ whenever $A_{i,j} = 1$ for all $i, j \in \mathbb{N}_{[1,m]}$ to form one algebraic relation among v and w. Similarly, the matrix $\bar{\Theta}(t) = \text{diag}(\Theta_i(t))_{i \in \mathbb{N}_{[1,m]}}$. The functions f_x, g_w, g_q, g_y are obtained by stacking $f_x^i, g_w^i, g_q^i, g_y^i$, respectively, in a column over all $i \in \mathbb{N}_{[1,m]}$. Furthermore, for each $m, n \in \{x, v, w, p, q, u, y\}$, $A_{mn}, B_{mn}, C_{mn}, D_{mn}$ are obtained by diagonally stacking $A_{mn}^i, B_{mn}^i, C_{mn}^i, D_{mn}^i$ over all $i \in \mathbb{N}_{[1,m]}$.

One can also view $\mathcal{P}_{\text{II}}$ and $\mathcal{P}_{\text{III}}$ as projections of $\mathcal{P}_{\text{I}}$ onto the subspaces spanned by the signals (x, c, d) and (x, c), respectively. To represent such projections using (8) and (9) requires elimination of interconnection signals $l(t)$ and print-job signals $d(t)$. The next theorem provides conditions under which such elimination of signals is possible.

Theorem III.1. (Model equivalence under signal elimination)

1) $\bar{\mathcal{P}}_{\text{II}} = \left\{(x, c, d) \mid \exists\ l \text{ such that } (x, c, l, d) \in \bar{\mathcal{P}}_{\text{I}}\right\}$ if and only if $(I - D_{wv}\bar{M})$ is invertible. Moreover, in that case,

$$\begin{bmatrix} A & B_1 & B_2 \\ C_1 & D_{11} & D_{12} \\ C_2 & D_{21} & D_{22} \end{bmatrix} = \begin{bmatrix} A_{xx} & B_{xp} & B_{xu} \\ C_{qx} & D_{qp} & D_{qu} \\ C_{yx} & D_{yp} & D_{yu} \end{bmatrix} + \begin{bmatrix} B_{xv} \\ D_{qv} \\ D_{yv} \end{bmatrix} \bar{M}(I - D_{wv}\bar{M})^{-1} \begin{bmatrix} C_{wx}^\top \\ D_{wp}^\top \\ D_{wu}^\top \end{bmatrix}^\top,$$
$$\begin{bmatrix} f(t) \\ g_1(t) \\ g_2(t) \end{bmatrix} = \begin{bmatrix} B_{xv} \\ D_{qv} \\ D_{yv} \end{bmatrix} \bar{M}(I - D_{wv}\bar{M})^{-1} \begin{bmatrix} f_x^\top(t) \\ g_q^\top(t) \\ g_y^\top(t) \end{bmatrix}^\top. \tag{10}$$

2) $\bar{\mathcal{P}}_{\text{III}} = \left\{(x, c) \mid \exists\ d \text{ such that } (x, c, d) \in \bar{\mathcal{P}}_{\text{II}}\right\} = \left\{(x, c) \mid \exists (l, d) \text{ such that } (x, c, l, d) \in \bar{\mathcal{P}}_{\text{I}}\right\}$ if and only if $(I - D_{11}\bar{\Theta}(t))$ is invertible for all $t \in \mathbb{T}$. Moreover, in that case,

$$\begin{bmatrix} \tilde{A}(t) & \tilde{B}(t) \\ \tilde{C}(t) & \tilde{D}(t) \end{bmatrix} = \begin{bmatrix} A & B_2 \\ C_2 & D_{22} \end{bmatrix} + \begin{bmatrix} B_1 \\ D_{21} \end{bmatrix} \bar{\Theta}(t)(I - D_{11}\bar{\Theta}(t))^{-1} \begin{bmatrix} C_1^\top \\ D_{12}^\top \end{bmatrix}^\top,$$
$$\begin{bmatrix} G(t) \\ J(t) \end{bmatrix} = \begin{bmatrix} B_1 \\ D_{21} \end{bmatrix} \bar{\Theta}(t)(I - D_{11}\bar{\Theta}(t))^{-1} \begin{bmatrix} f^\top(t) \\ g_2^\top(t) \end{bmatrix}^\top. \tag{11}$$

Proof: Deriving (10) requires algebraic manipulations to uniquely express v in terms of (x, u, p) by using $v(t) = \bar{M}w(t)$. The uniqueness of this expression requires the invertibility of $(I - D_{wv}\bar{M})$. The same argument holds for deriving (11), where d is uniquely expressed in terms of (x, u). In this case, one requires the invertibility of $(I - D_{11}\bar{\Theta}(t))$ for all $t \in \mathbb{T}$. ■

Remark III.1. (Assessment of the digital twin) The digital twin provides a modular modeling framework that is easily adjustable for an arbitrary number of nozzles. In fact, one simply requires to specify the number of nozzles and how they are distributed over rows. The digital twin then automatically builds the model of every individual nozzle due to their identical dimension and physical properties. The graph-theoretic approach leverages an easy re-adjustment of nozzles with the rest of the printhead components.

Lumping individual solid and liquid components may not always provide sufficient accuracy to the developed model. In this case, the digital twin is built to be flexible towards further partitioning individual components into multiple sub-components. Taking interconnection signals into account, it can be partitioned into smaller identical nodes until the required model accuracy is achieved in the graph. Once the

Preprints (www.preprints.org) | NOT PEER-REVIEWED | Posted: 22 April 2020 doi:10.20944/preprints202003.0355.v2

required model accuracy is achieved by partitioning, they are reconnected to the graph using interconnection relations.

Once the graph-theoretic model is built, the versatile digital twin offers four equivalent representations of the thermo-fluidic model if the conditions in theorem III.1 are satisfied. Based on the requirement whether it is design optimization of individual components, monitoring and fault diagnosis of nozzles, controller synthesis and deployment, the user has the freedom to choose any of these four representations. Typically, it is the hardware architecture, the purpose of the model or the time budget that decides the user's choice of a specific representation and this digital twin offers complete freedom.

IV. DEVELOPMENT AND CALIBRATION OF SOFT SENSOR

For control, monitoring, and fault-diagnosis of the thermo-fluidic processes, it is necessary to acquire real-time information about the liquid temperature. However, this must be achieved without incorporating any additional sensors. To this end, the piezoelectric elements, that are located at every individual nozzle, become useful. Apart from jetting liquid droplets, the self-sensing capability of the piezoelectric actuator (c.f. [15], [16]) is calibrated to make a sensing device from which liquid temperature can be estimated at every individual nozzle.

A. Mechanism of Acoustic Sensing

A piezoelectric element works in two operating modes. For jetting droplets of liquid, the piezoelectric element is in *actuation mode* where a sequence of trapezoidal voltage pulses allows droplet formation and ejection [17]. Using the same piezoelectric element, in *sensing mode*, one can capture the change in pressure oscillation and the nozzle acoustics during and after the actuation [18]. The mechanism is also known as *acoustic sensing* and the signal measured is called acoustic signal (Volt). The acoustic signal provides useful information about the dynamics inside a nozzle (c.f. [2], [4]).

By exploiting this self-sensing-actuation capability, in [2] and [15], two different approaches are presented to simultaneously operate the piezoelectric element in both actuation and sensing mode. However, these approaches require power-consuming and expensive electronic hardware that make it difficult for online implementation at every individual nozzle [4](Chapter 3). Moreover, these measurements are typically used for fault-diagnosis and monitoring of the nozzle acoustics. For simpler hardware and its online application as a temperature sensor, in this paper, a time delay (t_{delay}) is introduced between the actuation mode and sensing mode of the piezoelectric element. Once the actuation pulse is applied, after the time delay, an external trigger switches its operation to sensing mode, and the residual part of the acoustic signal is captured. Figure 4 depicts this sequential actuation-sensing scheme in an individual nozzle.

To use the piezoelectric element at every individual nozzle as a soft sensor for estimating liquid temperature, this paper uses the residual acoustic signal. By performing an experiment

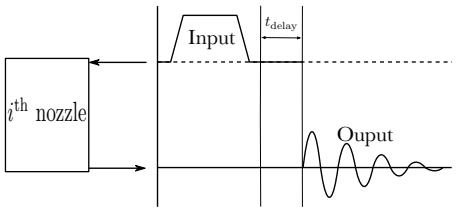

Fig. 4: Sequential scheme for acoustic sensing.

at liquid temperature T_1°C and T_2°C with $T_1 < T_2$, the corresponding acoustic sensing signals are measured and shown in figure 5. The difference in the measured signals indicates that the acoustic sensing signals can be used for estimating liquid temperature.

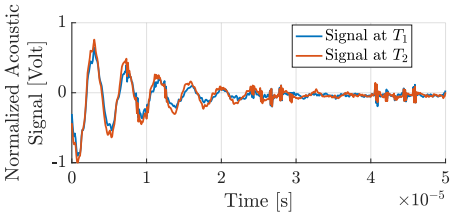

Fig. 5: Measured acoustic signal in a particular nozzle at two different liquid temperatures T_1, T_2.

B. Development of Soft Sensor

1) Reconstructing Acoustic Sensing Signal: In view of figure 5, one can assume that the acoustic sensing signal consists of discrete samples of a damped sinusoidal function:

$$y(n) = \alpha e^{-\zeta n T_s} \sin(\omega n T_s + \phi) + \gamma; \qquad n \in \mathbb{N}. \tag{12}$$

With a fixed sampling time T_s, $\alpha > 0$ denotes the amplitude (Volt), $0 < \omega < \pi$ the frequency (rad/sample), $-\pi < \phi \leq \pi$ the phase shift (rad), γ the signal offset (Volt) and $\zeta \geq 0$ the damping factor.

Let the finite samples of acoustic sensing signal are given as the set $\{s_n \mid n \in \mathbb{N}_{[1,N]}\}$, with the length of the data-set as $0 < N < \infty$ and the sampling period is fixed as T_s. The aim is to estimate the parameters α, ζ, ω, γ and ϕ such that (12) optimally approximates the measured signal $\{s_n \mid n \in \mathbb{N}_{[1,N]}\}$. To this end, the following algorithm is developed

Algorithm IV.1. (Reconstruction of acoustic sensing signal)

- *Model Hypothesis:* Consider a class of stable, second-order, single-input-single-output systems that has the following representation:

$$\begin{aligned} z(n+1) &= A_s z(n) + B_s w(n), \\ y(n) &= C_s z(n). \end{aligned} \tag{13}$$

  Here, for $n \in \mathbb{N} \cup \{0\}$, $z(n) \in \mathbb{R}^2$ is a vector with two internal states and $w(n) \in \mathbb{R}$ is the applied impulsive input. The output signal $y(n) \in \mathbb{R}$ is modeled as (12).
- *Estimation Algorithm:*

Preprints (www.preprints.org) | NOT PEER-REVIEWED | Posted: 22 April 2020 doi:10.20944/preprints202003.0355.v2

Algorithm 1 Estimating α, ζ, ω, γ and ϕ

Specify: T_s
Data: $\{s_n, n \in \mathbb{N}_{[1,N]}\}$
Unknowns: α, ζ, ω, γ, ϕ

Step 1 – Finding poles of the signal generating model

Specify: $L \leftarrow \lfloor \frac{N}{3} \rfloor$

Hankel matrix: $H \leftarrow \begin{bmatrix} s_1 & \dots & s_{L-1} & s_L \\ s_2 & \dots. & s_L & s_{L+2} \\ \vdots & \ddots & \vdots & \vdots \\ s_{N-L} & \dots. & s_{N-2} & s_{N-1} \\ s_{N-L+1} & \dots & s_{N-1} & s_N \end{bmatrix}$

Optimal 2-rank approximation of H (singular value decomposition):

$$H \approx U\Sigma V^{\mathrm{H}}, \quad \Sigma := \mathrm{diag}(\sigma_1, \sigma_2), \quad \sigma_1, \sigma_2 > 0$$

Define: $U^1 \leftarrow U[1 : N-L, :]$
Define: $U^2 \leftarrow U[2 : N-L+1, :]$
Determine: $\tilde{A}_s \leftarrow \Sigma^{-\frac{1}{2}} U^{1\dagger} U^2 \Sigma^{\frac{1}{2}}$
for $k = 1$ and 2 **do**
    Solve eigen value ρ_k and right eigen vector v_k:

$$(\tilde{A}_s - \rho_k) v_k = 0$$

    return ρ_k
end for

Step 2 – Determine ω and ζ

for $k = 1$ or 2 **do**
    $\omega \leftarrow \mathrm{Im}(\ln \rho_k)$
    $\zeta \leftarrow \mathrm{Re}(\ln \rho_k)$
end for
return ω, ζ

Step 3 – Determine α, ϕ, and γ

Define: $\mathbf{s} \leftarrow \mathrm{col}(s_1, \cdots, s_N)$
for $n \in \mathbb{N}_{[1,N]}$ **do**
    $\mathbf{\Gamma}[n, 1] \leftarrow (e^{j(\omega + j\zeta)nT_s} + e^{-j(\omega - j\zeta)nT_s})$
    $\mathbf{\Gamma}[n, 2] \leftarrow j(e^{j(\omega + j\zeta)nT_s} - e^{-j(\omega - j\zeta)nT_s})$
    $\mathbf{\Gamma}[n, 3] \leftarrow 1$
end for
Solve $\hat{\mathbf{x}} = \arg\min_{\mathbf{x}} ||\mathbf{\Gamma}\mathbf{x} - \mathbf{s}||_2$:

$$\hat{\mathbf{x}} \leftarrow (\mathbf{\Gamma}^{\mathrm{H}}\mathbf{\Gamma})^{-1}\mathbf{\Gamma}^{\mathrm{H}}\mathbf{s}$$

$\alpha \leftarrow 2\sqrt{\mathrm{Re}(\hat{\mathbf{x}}[1] + j\hat{\mathbf{x}}[2])^2 + \mathrm{Im}(\hat{\mathbf{x}}[1] + j\hat{\mathbf{x}}[2])^2}$
$\phi \leftarrow \mathrm{Im}(\ln(\hat{\mathbf{x}}[1] + j\hat{\mathbf{x}}[2]))$.
$\gamma \leftarrow \hat{\mathbf{x}}[3]$
return α, ϕ, γ

Proof: The proof as well as the accuracy of the algorithm are included in the supplementary material. ■

Here, reconstruction of (12) acts as a digital filter to improve the noise level on the measured signal. Furthermore, the estimation of α, ζ, ω, γ and ϕ also offers a online algorithm to monitor the dynamic behaviour inside every individual nozzle.

2) Estimation of Liquid Temperature Using Acoustic Energy: A next step would be to determine how individual parameter α, ζ, ω, γ or ϕ relates to the change in liquid temperature in a particular nozzle. Experiments show that the liquid temperature has the closest relation with the acoustic energy which is defined as the squared 2-norm of the estimated $y(n)$, $||y(n)||_2^2$. One expects lower acoustic energy in a lower temperature, and higher acoustic energy in a higher liquid temperature.

C. Calibration of Energy- Temperature Characteristics

To estimate liquid temperature, a characteristic relation between acoustic energy and liquid temperature needs to be established for an individual nozzle. This is achieved by performing the following three experiments consecutively.

1) Experiment 1: In the first experiment, three operating points are chosen for the liquid temperature. At a fixed operating point of temperature, the liquid droplets are jetted using the actuation mode of the piezoelectric element. After that, it is switched to sensing mode 20 times consecutively, and each time the acoustic sensing signal is measured. Every individual signal contains 100 samples of measured data. Using the measured data, the acoustic sensing signal is reconstructed using Algorithm IV.1, and its energy is computed. Based on this experiment, the energy-temperature curve is shown in figure 6. Despite the expected trend in change of acoustic energy with temperature, the variation of energy estimate is significantly large. Therefore, estimating liquid temperature using energy-temperature curve is still unreliable.

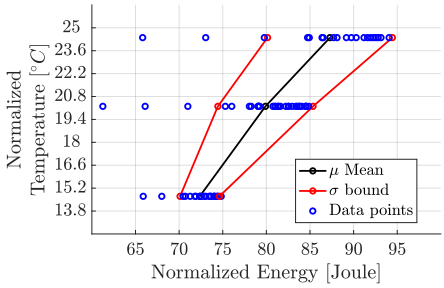

Fig. 6: Mean and variance of the energy-temperature curve at three operating points of liquid temperatures in Experiment 1.

2) Experiment 2: The evaporation of liquid changes its viscosity and temperature [14], and therefore also its acoustic energy. In order to present the consequence of evaporation, an experiment, similar to Experiment 1, is performed where four operating points of temperature are chosen. Liquid droplets are jetted at these operating temperature by using 2000 consecutive jetting pulses. The last jetting pulse is, thereafter, followed by switching the piezoelectric element in sensing mode and measuring a sequence of acoustic sensing signals. Here, the aim is to investigate the evolution of acoustic energy over time. In figure 7, the estimated acoustic energy of the acoustic signal is shown over one second. Over time, the effect of evaporation results in an initial decay of energy and the decay rate is higher if the temperature of the liquid droplet is higher.

Preprints (www.preprints.org) | NOT PEER-REVIEWED | Posted: 22 April 2020 doi:10.20944/preprints202003.0355.v2

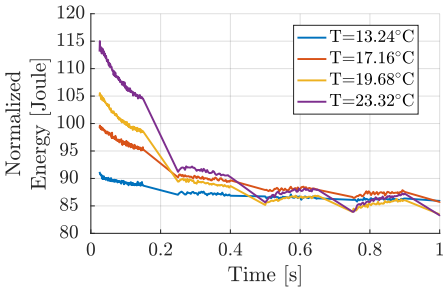

Fig. 7: Effect of evaporation on the estimated acoustic energy over time in Experiment 2.

This experiment implies that, due to evaporation, estimating the relation between temperature and acoustic energy depends on the timed sequence between jetting and sensing. In other words, the larger the difference between the time of jetting pulses and the time of measurements, the lower the acoustic energy. As a result, the estimation method based on this experiment has a poor signal-to-noise ratio.

3) Experiment 3: To circumvent the effect of evaporation from the energy-temperature relation, only those acoustic sensing signals should be considered that are measured immediately after the jetting pulse. To this end, another experiment is performed where the liquid temperature is varied over four operating points. In contrast to the previous experiments where a series of acoustic signals are measured one after another, this time, jetting of the liquid droplet is directly followed by the sensing of the acoustic signal. This sequence of consecutive jetting and sensing is repeated 20 times. Using the measured data, the acoustic energy is estimated. Figure 8 shows that the adapted approach of consecutive jetting-sensing significantly improves the variance in the estimate of energy-temperature relation.

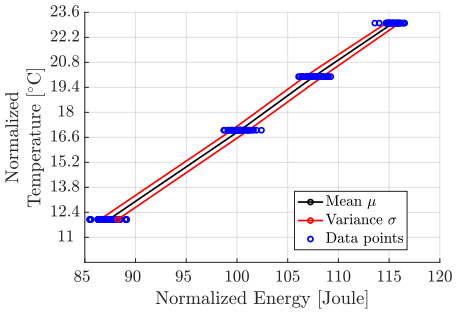

Fig. 8: Relation between the liquid temperature of a nozzle and estimated acoustic energy in Experiment 3.

In figure 9-10, the designs of Experiment 1 and Experiment 3 are compared, respectively. The key difference between them is the sequence in which jetting actuation and acoustic sensing are performed. Based on the sequential jetting-sensing mechanism devised in Experiment 3, the energy-temperature characteristic curves are estimated and calibrated for every individual nozzle. In figure 11, energy-temperature curves are shown for four different nozzles in the printhead.

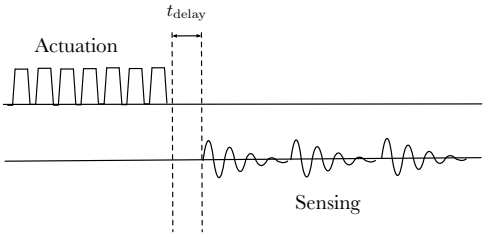

Fig. 9: Actuation-sensing sequence in Experiment 1.

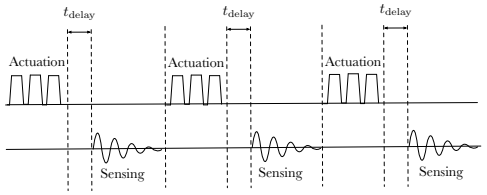

Fig. 10: Actuation-sensing sequence in Experiment 3.

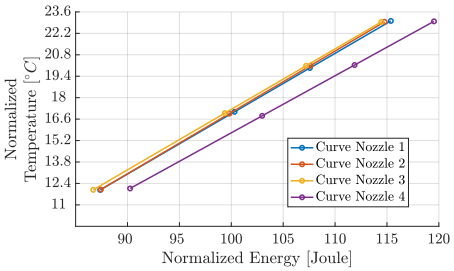

Fig. 11: Estimation of energy-temperature curve for four nozzles.

D. Estimation of Liquid Temperature Using Energy-Temperature Curve

Based on the energy-temperature curves, one can determine a parametric linear model relating the acoustic energy and the liquid temperature. For an individual nozzle, let the energy-temperature characteristic curve be modeled as:

$$x_i = m_i \phi_i + c_i. \tag{14}$$

Here, for i^{th} nozzle, x_i is the liquid temperature and ϕ_i is the acoustic energy. The unknown parameters $m_i, c_i \in \mathbb{R}$ are obtained by fitting the respective energy-temperature curve. Every time a liquid droplet is jetted from a nozzle, thereafter, it can be followed by measuring the acoustic signal. The acoustic signal is modeled as (12) and its energy ϕ_i is determined using Algorithm IV.1. Subsequently, the corresponding liquid temperature x_i is obtained from (14).

V. EXPERIMENTAL VALIDATION

A. Experimental Setup

To validate the digital twin as well as the soft sensor, an experimental set-up is built, as shown in figure 12. The set-up consists of two liquid vessels that are connected with a printhead that has 160 nozzles. By keeping two vessels at a fixed level, a constant re-circulation flow through the printhead is established. To raise the temperature of the liquid inlet in

Preprints (www.preprints.org) | NOT PEER-REVIEWED | Posted: 22 April 2020 doi:10.20944/preprints202003.0355.v2

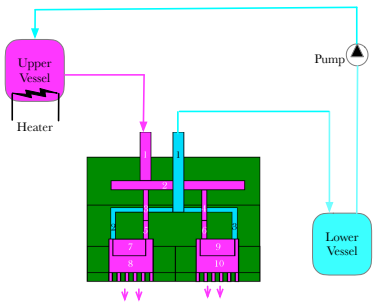

Fig. 12: Experimental Setup.

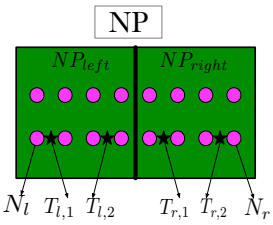

Fig. 13: Bottom configuration of NP with thermo-couples ($\star$).

the printhead, the upper vessel is equipped with a heater. For each side of the NP, two locations are selected to place thermo-couples (in figure 13 they are called $T_{l,1}, T_{l,2}$ for NP_{left} and $T_{r,1}, T_{r,2}$ for NP_{right}) to receive real-time information of its temperature. These thermo-couples are used solely for validation purpose and are not allowed in the final product. Moreover, at each side of NP, one nozzle is selected whose temperature is monitored using the developed soft sensor (in figure 13 they are called N_l for NP_{left} and N_r for NP_{right}). In this way, temperature evolution of both solid and liquid are measured on the both side of the printhead.

B. Experiment Design

The printhead is operated to print 3500 A-4 sheets of paper. Only the nozzles in NP_{left} are actuated for jetting while keeping the nozzles in NP_{right} idle. The bit-map is designed such that

1) For 100 seconds, first 500 pages are left unprinted.
2) In the next 100 seconds, another 500 pages are entirely printed by using all the nozzles in NP_{left}.
3) In the next 100 seconds, another 500 pages are left unprinted.
4) In the next 100 seconds, another 500 pages are entirely printed by using half of the nozzles that are located on the left side of NP_{left}.
5) In the next 100 seconds, 500 pages are left unprinted.
6) In the next 100 seconds, another 500 pages are entirely printed by using half of the nozzles that are located on the right side of NP_{left}.
7) In the next 100 seconds, the last 500 pages are left unprinted.

C. Setting Up The Digital Twin for Simulation

Based on the bit-map, corresponding flow parameters are assigned with the print-job signals. With 160 nozzles, a graph theoretical digital twin of the printhead is built by following the nodal structure that is depicted in figure 2. Every individual node is associated with its temperature (in °C) as its internal state. Based on the topology of the printhead, the interconnection signals and their relations are built. The print-job also assigns the flow parameters to every individual node through the print-job signals and their relations. Once the model is built using the definitions (D.1)-(D.3), any one of the representations $\mathcal{P}_{\text{I}}$, $\mathcal{P}_{\text{III}}$, $\mathcal{P}_{\text{III}}$ can be used for simulating the digital twin.

D. Results

In figure 14, at location $T_{l,1}, T_{l,2}$ and $T_{r,1}, T_{r,2}$, temperature data measured by the thermo-couples are compared against the temperatures of the corresponding nodes simulated by the digital twin. Using the developed soft sensor, in figure 15, the estimated liquid temperature at N_l and N_r are compared against the temperatures of the corresponding nodes simulated by the digital twin. The developed model captures the thermo-

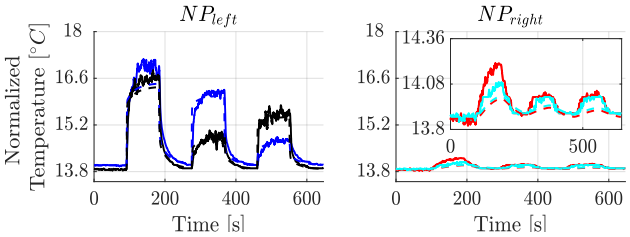

Fig. 14: Comparisons among the temperature measurements from the thermo-couple and the digital twin. The legends are as follows: temperature at $T_{l,1}$; temperature at the corresponding node in the digital twin; temperature at $T_{l,2}$; temperature at the corresponding node in the digital twin; temperature at $T_{r,1}$; temperature at the corresponding node in the digital twin; temperature at $T_{r,2}$; temperature at the corresponding node in the digital twin.

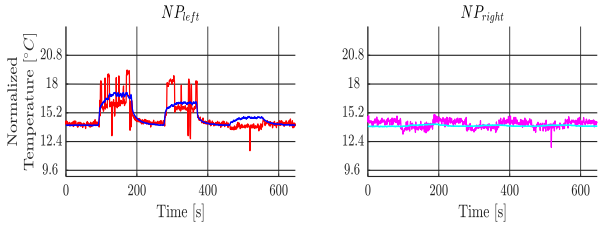

Fig. 15: Comparisons of nozzle temperature among the estimates of the developed soft sensor and the digital twin. The legends are as follows: estimated temperature of N_l by soft sensor; temperature at the corresponding node in the digital twin; estimated temperature of N_r by soft sensor; temperature at the corresponding node in the digital twin.

fluidic behaviour of the printhead by indicating the offset in temperature among jetting and non-jetting nozzles. For example, as the nozzles in NP_{right} are idle during the entire

Preprints (www.preprints.org) | NOT PEER-REVIEWED | Posted: 22 April 2020 doi:10.20944/preprints202003.0355.v2

print-job, its temperature variation is significantly smaller. Nevertheless, there is still a small temperature variation for nozzles in NP_{right} due to thermo-fluidic cross-talk among nozzles. Using only the left half of the nozzles or the right-half of the nozzles in NP_{left}, among nozzles, there is a significant temperature difference over time (around $2°C$ difference between $T_{l,1}$ and $T_{l,2}$ during $300-400$ seconds). The role of the liquid re-circulation is also evident as the temperatures of the NP always go to a steady-state value while being idle.

Similarly, in figure 15, the soft sensor's estimation of the liquid temperature follows the same trend that of the digital twin. The sudden oscillations that appear in the soft sensor's estimation are due to sporadic bubble entrapment or drying of liquid inside the nozzle during jetting, which may fluctuate the liquid temperature. Such erratic phenomena are not captured in the digital twin. On the other hand, the non-jetting nozzles' temperature estimation is almost identical to the model.

VI. IN SITU CONTROLLER: A PROOF OF PRINCIPLE

The performance limiting aspects of thermo-fluidic processes is the fluctuation in liquid temperature among adjacent nozzles in a printhead and among adjacent printheads. To maintain temperature consistency, a controller is synthesized that does not require incorporating any additional sensor or actuator. The only resources the controller uses are a) the bit-map as prior knowledge about the flow pattern and jetting sequence of nozzles in the printhead, b) the model derived in Section III to anticipate and predict the evolution of thermo-fluidic behaviour in the printhead, and c) the soft sensor as feedback information on temperature and viscosity at every nozzle as derived and discussed in Section IV.

A. Concept of In Situ Sensing-Actuation

Every individual nozzle is equipped with a piezoelectric element for jetting droplets of liquid. By applying a voltage, its resistive property allows the piezoelectric element to dissipate heat. In this controller design problem, the resistive property of a jetting actuator is used as a source of heating. Thus, the piezoelectric element makes every individual nozzle equipped with a local, independent, *in situ* self-sensing heating actuator.

However, the piezoelectric elements can only be used as heaters for control input when there is no need for jetting liquid. To implement the in situ sensing-actuation scheme, at all time $t \in \mathbb{T}$, every individual nozzle is in either jetting, heating, sensing or idle mode. To allocate the nozzles in these four modes of operations, following time-varying set-valued maps are defined:

1) $\mathbb{S}_p(t)$: The set of all nozzles that are used for jetting liquid droplets at time t. The cardinality of the set is $n_p(t)$.
2) $\mathbb{S}_h(t)$: The set of all nozzles that are non-jetting and are used as heaters at time t. The cardinality of the set is $n_h(t)$.
3) $\mathbb{S}_s(t)$: The set of all nozzles whose temperatures are sensed at time t. The cardinality of the set is $n_s(t)$.
4) $\mathbb{S}_u(t)$: The set of all nozzles that are neither in any of the above modes at time t. The cardinality of the set is $n_u(t)$.

The cardinality of each set (as a function of time) depends on a specific bit-map. Intersections of $\mathbb{S}_p(t)$ and $\mathbb{S}_h(t)$ must be empty for all time $t \in \mathbb{T}$. This requirement on functional exclusion is a serious engineering challenge as a piezoelectric element in heating mode is not supposed to jet. As described in Section IV, there is always a delay between applying the jetting pulse and sensing the temperature using a soft sensor. Therefore, the jetting nozzles are chosen not to be used for sensing (i.e. the intersection between $\mathbb{S}_p(t)$ and $\mathbb{S}_s(t)$ is chosen to be empty).

B. Performance Specifications

The controller must satisfy the following performance specifications:

1) Irrespective of the bit-map, the differences in temperature among adjacent nozzles must be below $\pm 0.3°$C.
2) The usage of thermal actuation must be limited to sustain operational lifetime of piezoelectric elements.
3) Cooling of the liquid is not possible using the thermal actuation.
4) Thermal actuation of piezoelectric material should be non-jetting, i.e. it should not form new droplets of liquid.

Intuitively, using the in situ sensing-actuation scheme, the controller is expected to actuate only on a few heating nozzles (from the set $\mathbb{S}_h(t)$) adjacent to the jetting ones to limit the temperature difference among nozzles while satisfying the performance specifications. At the same time, the nozzles' temperature can be monitored using the implemented soft sensor at the sensing nozzles (from the set $\mathbb{S}_s(t)$).

C. Generating Voltage Pulse for Heating Actuators

To apply the required amount of thermal power as control inputs, one needs to design voltage pulses that are to be applied on the piezoelectric elements in heating mode. Such voltage pulse must not cause ejection of droplets while satisfying the power requirement. The principle behind generating a non-jetting and heating voltage pulse is to modulate the amplitude and frequency of the trapezoidal pulses (c.f. [19]). Recently, in [20], a mechanism is developed so as to generate specific thermal energy while not interfering with the bandwidth that defines the jetting mode. Using band-pass modulation, the width and the height of the trapezoidal voltage pulses are tuned. Further details on these signal implementations are omitted for brevity.

D. Model-Based Prediction of Liquid Temperature in Nozzles

As mentioned in Section III, there are four equivalent ways to represent the model of thermo-fluidic processes and one has the freedom to use any one of them for predicting the future evolution of liquid temperature in nozzles. Here, the thermo-fluidic behaviour is considered to be represented according to $\mathcal{P}_{\text{III}}$ in (9). In discrete time, i.e. for $t \in \{kt_d | k \in \mathbb{N} \cup \{0\}\}$, the behaviour of $\mathcal{P}_{\text{III}}$ is governed by the following equations:

$$\begin{bmatrix} Q_t(x)(t) \\ y(t) \end{bmatrix} = \begin{bmatrix} \tilde{A}(t) & \tilde{B}(t) \\ \tilde{C}(t) & \tilde{D}(t) \end{bmatrix} \begin{bmatrix} x(t) \\ u(t) \end{bmatrix} + \begin{bmatrix} G(t) + W(t)d(t) \\ J(t) \end{bmatrix}. \tag{15}$$

Preprints (www.preprints.org) | NOT PEER-REVIEWED | Posted: 22 April 2020 doi:10.20944/preprints202003.0355.v2

Here, $Q_t(x)(t) := x(t+t_d), t \in \{kt_d | k \in \mathbb{N} \cup \{0\}\}$. If there are n_{nozzle} number of nozzles in the pinthead, $u(t), y(t) \in \mathbb{R}^{n_{\text{nozzle}}}$.

During jetting, the actuation of jetting piezoelectric actuators causes heat dissipation [19]. Given the amplitude and frequency of the voltage pulses, one can experimentally estimate the thermal power (in Watt) generated in jetting nozzles over time, and they are modeled as known disturbances $d(t) \in \mathbb{R}^{n_{\text{nozzle}}}$.

However, to implement the in situ sensing-actuation scheme, the bit-map allocates the nozzles according to the four modes of operation defined in Section VI.A. To map the total number of nozzles to its allocated modes of operation, binary matrices $S^p(t) \in \mathbb{R}^{n_{\text{nozzle}} \times n_p(t)}$, $S^h(t) \in \mathbb{R}^{n_{\text{nozzle}} \times n_h(t)}$, and $S^s(t) \in \mathbb{R}^{n_s(t) \times n_{\text{nozzle}}}$ are introduced. Their (i,j)-th entries are:

$$S^p_{i,j}(t) = \begin{cases} 1, & i \in \mathbb{S}_p(t), \quad j \in \mathbb{N}_{[1,n_p(t)]} \\ 0, & \text{otherwise.} \end{cases},$$

$$S^h_{i,j}(t) = \begin{cases} 1, & i \in \mathbb{S}_h(t), \quad j \in \mathbb{N}_{[1,n_h(t)]} \\ 0, & \text{otherwise.} \end{cases},$$

$$S^s_{i,j}(t) = \begin{cases} 1, & i \in \mathbb{N}_{[1,n_s(t)]}, \quad j \in \mathbb{S}_s(t) \\ 0, & \text{otherwise.} \end{cases},$$

As a result, (15) is modified as

$$\begin{bmatrix} (Q_t(x))(t) \\ y^s(t) \end{bmatrix} = \begin{bmatrix} \tilde{A}(t) & \tilde{B}(t)S^h(t) \\ S^s(t)\tilde{C}(t) & S^s(t)\tilde{D}(t)S^h(t) \end{bmatrix} \begin{bmatrix} x(t) \\ u^h(t) \end{bmatrix} + \begin{bmatrix} G(t) + W(t)S^p(t)d^p(t) \\ J(t) \end{bmatrix}. \quad (16)$$

Here, at time $t \in \mathbb{T}$, the control inputs $u^h(t) \in \mathbb{R}^{n_h(t)}$ are applied by the set of heating nozzles (in terms of thermal power, Watt). The disturbance due to jetting $d^p(t) \in \mathbb{R}^{n_p(t)}$ are applied by the set of jetting nozzles (in terms of thermal power, Watt). The sensed outputs $y^s(t) \in \mathbb{R}^{n_s(t)}$ are sensed liquid temperature by the set of sensing nozzles (in terms of temperature, °C).

E. Formulating Operational Constraints

Let $u_{\max} \in \mathbb{R}^{n_{\text{nozzle}}}$ be the maximum admissible thermal power of all piezoelectric elements. Here, $u_{\max}$ is determined such that it takes the degradation of piezoelectric elements into account, while preventing the ejection of droplets of liquid. On the other end, cooling is not allowed. As a result, at every time instant $t \in \mathbb{T}$, heating piezoelectric elements must satisfy the constraint

$$0 \leq S^h(t)u^h(t) \leq u_{\max}. \quad (17)$$

Having bounded actuation and bounded thermal disturbance during jetting, no additional constraints on the state variable $x(t)$ has been enforced.

F. Specifying Control Criterion

The purpose of the controller is to control the temperature difference among nozzles. They are defined by a vector of to-be-controlled variables

$$z(t) = Hx(t), \quad (18)$$

where, z denotes the vector of all temperature differences among individual adjacent nozzles. In particular, $H \in \mathbb{R}^{n_x \times n_x}$ is a sparse matrix with $H_{i,i} = 1$ and $H_{i,j} = -1$ whenever the i^{th} nozzle is adjacent to the j^{th} nozzle.

At every time instant $t = kt_d$ with $k \in \mathbb{N} \cup \{0\}$, the requirement is to control the liquid temperature gradient among nozzles over a finite horizon of future time instants $t \in \mathbb{T}^k_N$ where $\mathbb{T}^k_N := \{kt_d \mid k \in \mathbb{N}_{[k,N+k]}\}$ for $N > 0$. To this end, a reference tracking problem is formulated to minimize the following cost functional:

$$J_k := \sum_{t \in \mathbb{T}^k_N} ||x(t) - x^r||^2_{Q_k(t)} + \sum_{t \in \mathbb{T}^k_{N-1}} ||u^h(t) - u^r(t)||^2_{R_k(t)}. \quad (19)$$

Here, the reference trajectories $(x^r, u^r(t))$ are pre-determined from a steady state model that equates the temperature difference of nozzles to zero. In other words, for $t \in \mathbb{T}^k_N$, $(x^r, u^r(t))$ is the solution of the following linear equations:

$$\begin{aligned} x^r &= \tilde{A}(t)x^r + \tilde{B}(t)S^h(t)u^r(t) + G(t) + W(t)S^p(t)d^p(t), \\ 0 &= Hx^r. \end{aligned} \quad (20)$$

Moreover, for all $t \in \mathbb{T}^k_N$, one must pre-define the time-varying weights $Q_k(t) \in \mathbb{R}^{n_x \times n_x}, R_k(t) \in \mathbb{R}^{n_h(t) \times n_h(t)}$ in (19) to penalize the deviation of states and inputs from their respective references.

G. Formulating Model Predictive Control Scheme

A digital controller is required that minimizes (19) by using future prediction on the states in (16) while satisfying the constraints in (17). To this end, a reference-tracking model predictive control (MPC) scheme is presented.

At every time instant $t = kt_d$ with $k \in \mathbb{N} \cup \{0\}$, for convenience, let any function $f(t)$ be defined as $f_{0|k} := f(kt_d)$. From its initial value $f_{0|k}$, over a finite horizon of future time instants $t \in \mathbb{T}^k_N$ with $N > 0$, the value of $f(t)$ at instant $k+i$ is denoted by $f_{i|k} := f((k+i)t_d)$. Starting from the time step kt_d, the N-horizon MPC scheme amounts to minimizing the following cost functional (c.f. [21])

$$J(k, \bar{x}_k, \bar{u}^h_k) := ||x_{N|k} - x^r||^2_{Q_k} + \sum_{i=0}^{N-1} \left(||x_{i|k} - x^r||^2_Q + ||u^h_{i|k} - u^r_{i|k}||^2_{R_{i|k}} \right), \quad (21)$$

subject to the following constraints:

$$x_{i+1|k} = \tilde{A}_{i|k}x_{i|k} + \tilde{B}_{i|k}S^h_{i|k}u^h_{i|k} + \tilde{G}_{i|k}, i \in \mathbb{N}_{[0,N-1]}, \quad (22a)$$

$$E_{i|k}u^h_{i|k} \leq b, \quad i \in \mathbb{N}_{[0,N-1]}, \quad (22b)$$

$$F_{N|k}x_{N|k} \leq b_{N|k}, \quad (22c)$$

$$x_{0|k} = x(kt_d). \quad (22d)$$

Here, for $i \in \mathbb{N}_{[0,N-1]}$,

$$\begin{aligned} \tilde{G}_{i|k} &= G_{i|k} + W_{i|k}S^p_{i|k}d^p_{i|k}, \\ E_{i|k} &= \text{col}(-S^h_{i|k}, S^h_{i|k}), \\ b &= \text{col}(0, u_{\max}). \end{aligned}$$

Preprints (www.preprints.org) | NOT PEER-REVIEWED | Posted: 22 April 2020 doi:10.20944/preprints202003.0355.v2

For all $t \in \mathbb{T}_N^k$, the reference trajectories (x^r, u^r) are determined by solving (20). The weights $Q \in \mathbb{R}^{n_x \times n_x}, R_{i|k} \in \mathbb{R}^{n_h(t) \times n_h(t)}$ are user-defined matrices. The terminal penalty $Q_k \in \mathbb{R}^{n_x \times n_x}$ in the cost (21) and $F_{N|k}, b_{N|k}$ in the terminal constraint (22c) are specifically chosen to ensure stability of the closed-loop system [22].

The above constrained optimization problem is solved for every k over the horizon $kt_d, \dots (k+N)t_d$ of N future time samples. The sequence of predicted states and future inputs are denoted as $\bar{x}_k := \{x_{1|k}, \cdots, x_{N|k}\}$ and $\bar{u}_k^h := \{u_{0|k}^h, \cdots, u_{N-1|k}^h\}$ respectively. If the minimizer of the optimal control problem (21)-(22) is denoted by $\bar{u}_k^{h*} := \{u_{0|k}^{h*}, \cdots, u_{N-1|k}^{h*}\}$, then its first entry $u_{0|k}^{h*}$ is implemented as control input at time step $t = kt_d$. Subsequently, on a receding horizon, the optimal control problem is solved again at step $(k+1)t_d$ using $x_{0|k+1} = x((k+1)t_d)$ as its initial state. In a receding horizon fashion, this procedure is continued iteratively over all time $t \in \{kt_d \mid k \in \mathbb{N} \cup \{0\}\}$ [23].

One may substitute the equality constraint (22a) in (21) to eliminate the variables $\{x_{0|k}, \cdots, x_{N|k}\}$. This results in the following dense linearly constrained quadratic programming (LCQP) problem:

Optimization Problem 1. (Dense LCQP)

$$\arg\min_{U_k} \ \frac{1}{2} U_k^\top G_k U_k + U_k^\top W_k \tag{23a}$$

$$\text{subject to } L_k U_k \leq V_k, \tag{23b}$$

where,

$$\begin{aligned}
G_k &= 2(\Gamma_k^\top \Omega_k \Gamma_k + \Psi_k),\\
W_k &= (2\Gamma_k^\top \Omega_k \Phi_k) x_{0|k} + 2\Gamma_k^\top \Omega_k \Xi_k - \Lambda_k,\\
\Lambda_k &= -2\Gamma_k^\top \Omega_k X_k^r - 2\Psi_k U_k^r,\\
L_k &= \bar{M}\Gamma_k + \bar{E}_k,\\
V_k &= \bar{b} - \bar{M}\Phi_k x_{0|k} - \bar{M}\Xi_k,\\
x_{0|k} &= x(k),
\end{aligned}$$

with

$$\Phi_k = \begin{bmatrix} \tilde{A}_{0|k} \\ \tilde{A}_{1|k}\tilde{A}_{0|k} \\ \vdots \\ \tilde{A}_{N-1|k} \cdots \tilde{A}_{0|k} \end{bmatrix}, \bar{M} = \begin{bmatrix} 0 & \cdots & 0 \\ 0 & \cdots & 0 \\ \vdots & \ddots & \vdots \\ 0 & \cdots & F_{N|k} \end{bmatrix},$$

$$\bar{E}_k = \begin{bmatrix} E_{0|k} & \cdots & 0 \\ \vdots & \ddots & \vdots \\ 0 & \cdots & E_{N-1|k} \\ 0 & \cdots & 0 \end{bmatrix}, \bar{b} = \begin{bmatrix} b \\ b \\ \vdots \\ b_{N|k} \end{bmatrix},$$

$$\Gamma_k = \begin{bmatrix} \tilde{B}_{0|k} & 0 & \cdots & 0 \\ \tilde{A}_{1|k}B_{0|k} & \tilde{B}_{1|k} & \cdots & 0 \\ \vdots & \vdots & \ddots & \vdots \\ \tilde{A}_{N-1|k} \cdots \tilde{A}_{1|k}\tilde{B}_{0|k} & \tilde{A}_{N-2} \cdots \tilde{A}_{2|k}\tilde{B}_{1|k} & \cdots & \tilde{B}_{N-1|k} \end{bmatrix}$$

$$\Xi_k = \begin{bmatrix} \tilde{G}_{0|k} & 0 & \cdots & 0 \\ \tilde{A}_{1|k}\tilde{G}_{0|k} & \tilde{G}_{1|k} & \cdots & 0 \\ \vdots & \vdots & \ddots & \vdots \\ \tilde{A}_{N-1|k} \cdots \tilde{A}_{1|k}\tilde{G}_{0|k} & \tilde{A}_{N-2|k} \cdots \tilde{A}_{2|k}\tilde{G}_{1|k} & \cdots & \tilde{G}_{N-1|k} \end{bmatrix} \begin{bmatrix} 1 \\ 1 \\ \vdots \\ 1 \end{bmatrix}.$$

Here, the decision variables are the to-be-applied control input $U_k = \text{col}(u_{0|k}^h, \cdots, u_{N-1|k}^h)$. Moreover, $X_k^r = \text{col}(x^r, \cdots, x^r)$ and $U_k^r = \text{col}(u_{0|k}^r, \cdots, u_{N-1|k}^r)$ are the reference values for states and inputs respectively. Moreover, $\Psi_k := \text{diag}(R_{0|k}, \cdots, R_{N-1|k})$ and $\Omega_k := \text{diag}(Q, \cdots, Q, Q_k)$.

The following result summarizes convergence properties of the resulting controlled system.

Theorem VI.1. (Stability of the in situ controller) Let the matrices $R_{i|k} \in \mathbb{S}_{\succ 0}^{n_h(t)}$, $Q \in \mathbb{S}_{\succ 0}^{n_x}$ are given for all time $t \in \mathbb{T}_N^k$. Moreover, $X_k \in \mathbb{S}_{\succ 0}^{n_x}$ and $Y_k \in \mathbb{R}^{n_h(t) \times n_x}$ satisfy the following linear matrix inequality (LMI)

$$\begin{pmatrix} -X_k & 0 & \tilde{A}_{N|k}X_k + \tilde{B}_{N|k}Y_k & 0 \\ 0 & -R_{N|k}^{-1} & Y_k & 0 \\ (\tilde{A}_{N|k}X_k + \tilde{B}_{N|k}Y_k)^\top & Y_k^\top & -X_k & X_k \\ 0 & 0 & X_k & -Q^{-1} \end{pmatrix} \preccurlyeq 0. \tag{24}$$

Furthermore, let (23) have a unique minimizer $U_k^* := \{u_{0|k}^{h*}, \cdots, u_{N-1|k}^{h*}\}$ under the following conditions:

1) The terminal weight matrix Q_k admits $Q_k = X_k^{-1}$
2) The terminal constraint $F_{N|k}x_{N|k} \leq b_{N|k}$ admits

$$F_{N|k} = E_{N|k}K_k; \quad b_{N|k} = b - u_{N|k}^r + E_{N|k}K_k x^r,$$

where, $K_k = Y_k X_k^{-1}$, $E_{N|k} = \text{col}(-S_{N|k}^h, S_{N|k}^h)$, and $b = \text{col}(0, u_{\max})$.

Then, setting $u^h(kt_d) = u_{0|k}^{h*}$, there exists a $\delta > 0$ for which every initial condition $||x(0) - x^r||_2 < \delta$ and every solution to (16), $k \to x(kt_d)$, admits $\lim_{k\to\infty} ||x(kt_d) - x^r||_2 = 0$.

Proof: The proof is included in the supplementary material. ■

H. Implementation and Illustration of MPC Scheme

As proof of principle, the presented MPC scheme is implemented to minimize the difference in liquid temperature among nozzles. To this end, the following specifications are considered:

1) Printhead Configuration: The printhead chosen for implementing MPC has the architecture shown in figure 1a. There are 48 nozzles that are equally divided over two-sides of the NP, and at each side, 24 nozzles are equally distributed over two rows.

2) Bit-map Specification: For generating a test bit-map, the following scenarios are considered:

- Scenario 1: All 24 nozzles that located in NP_{left} are used as a jetting nozzle.
- Scenario 2: 12 nozzles in NP_{right} that are located closest to the NP_{left} are used as jetting nozzle.
- Scenario 3: 12 nozzles in NP_{right} that are located farthest from the NP_{left} are used as jetting nozzle.

3) Setting Up the Digital Twin of the Model: Based on the above scenarios, the flow parameters are assigned to every individual node. At the same time, the thermal power dissipated by the individual jetting nozzle is used as known disturbances.

Preprints (www.preprints.org) | NOT PEER-REVIEWED | Posted: 22 April 2020 doi:10.20944/preprints202003.0355.v2

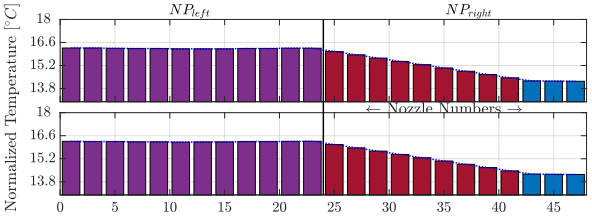

(a) Controlled Scenario 1: NP_{left} is fully used for jetting. Maximum absolute difference of temperature between two adjacent nozzles is $\mathbf{0.1988}^{\circ}C$.

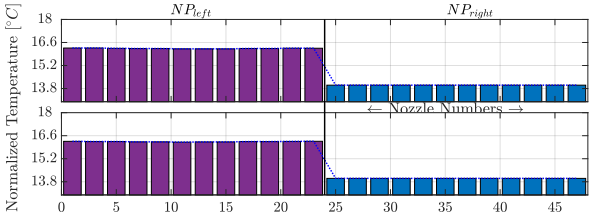

(b) Uncontrolled Scenario 1: NP_{left} is fully used for jetting. Maximum absolute difference of temperature between two adjacent nozzles is $\mathbf{2.2551}^{\circ}C$.

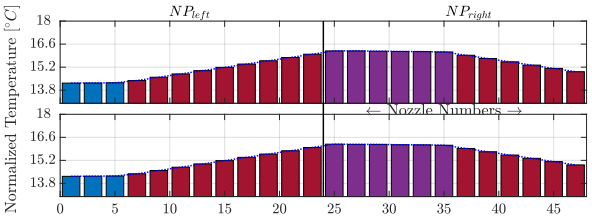

(a) Controlled Scenario 2: Left half of NP_{right} is used for jetting. Maximum absolute difference of temperature between two adjacent nozzles is $\mathbf{0.2}^{\circ}C$.

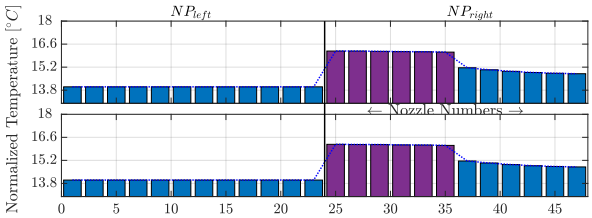

(b) Uncontrolled Scenario 2: Left half of NP_{right} is used for jetting. Maximum absolute difference of temperature between two adjacent nozzles is $\mathbf{2.1726}^{\circ}C$.

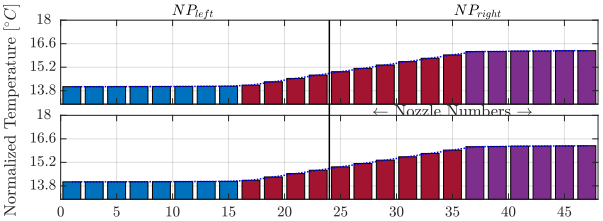

(a) Controlled Scenario 3: Right half of NP_{right} is used for jetting. Maximum absolute difference of temperature between two adjacent nozzles is $\mathbf{0.2}^{\circ}C$.

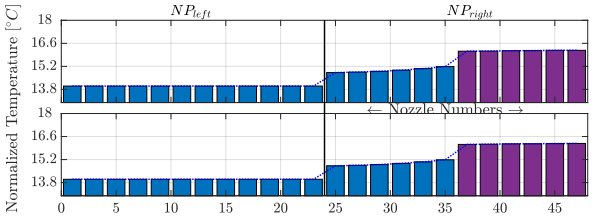

(b) Uncontrolled Scenario 3: Right half of NP_{right} is used for jetting. Maximum absolute difference of temperature between two adjacent nozzles is $\mathbf{0.9368}^{\circ}C$.

Fig. 18: Liquid temperature of 48 nozzles for three scenarios in controlled and uncontrolled case. ■ denotes nozzles that are jetting. ■ denotes the adjacent nozzles that are used as thermal actuators. ■ denotes the nozzles that are not used for heating.

The model of every individual node is considered in discrete time by choosing the $\mathbb{T} = \{kt_d \mid k \in \mathbb{N} \cup \{0\}\}$ with $t_d = 0.01$ seconds. Euler's approach is used for time discretization due to its sparse and structure preserving implementation ([24], page 4).

The thermo-fluidic model is defined as a graph following the definitions (D.1)-(D.3) in Section III. The equivalent representations $\mathcal{P}_{\text{II}}$ and $\mathcal{P}_{\text{III}}$ are determined by eliminating the interconnection and print-job signals.

The in situ sensing-actuation scheme, as discussed in Section VI.A is implemented by allocating the nozzles based on their four modes operations. The set $\mathbb{S}_p(t)$ determines the set of all jetting nozzles. The rest of nozzles, except the three nozzles that are located at the furthest distance from the jetting nozzles, are used for heating. This determines $\mathbb{S}_h(t)$. All the nozzles that do not belong to $\mathbb{S}_p(t)$ are used as soft sensors to estimate the change in liquid temperature. With the allocated nozzles, the matrices $S^h(t), S^p(t), S^s(t), S^u(t)$ are built. The model for control (16) is built subsequently. The unmeasured states are automatically replaced by the corresponding state-updates from the model.

4) Solving MPC Scheme: Using (16), The prediction model is built over the time horizon $t \in \mathbb{T}_N^k$ where $\mathbb{T}_N^k := \{kt_d \mid k \in \mathbb{N}_{[k,N+k]}\}$. Here, $N = 8$. In (21), the weights Q and $R_{i|k}$ are chosen as diagonal matrices. Here, the diagonal entries in $R_{i|k}$ are chosen significantly higher than that of Q to strictly penalize the deviation of inputs from its reference values. Moreover, entries of $R_{i|k}$ are chosen such that the heating nozzles adjacent to the jetting nozzles have more input power.

The optimization problem in (23) is solved by the freely available `mpcqpsolver` using the interior point method. Once the optimization yields the optimal control inputs, they are applied to the heating piezoelectric actuators by means of non-jetting voltage pulses. The MPC then repeats the same procedure over the entire bit-map iteratively.

5) Results: Once the MPC is applied, the liquid temperatures of all 48 nozzles are shown in figure 18. It demonstrates that the performance specifications are met while satisfying the constraints. Moreover, only the adjacent heating nozzles are used to compensate for the temperature inconsistencies among jetting and non-jetting nozzles.

Preprints (www.preprints.org) | NOT PEER-REVIEWED | Posted: 22 April 2020 doi:10.20944/preprints202003.0355.v2

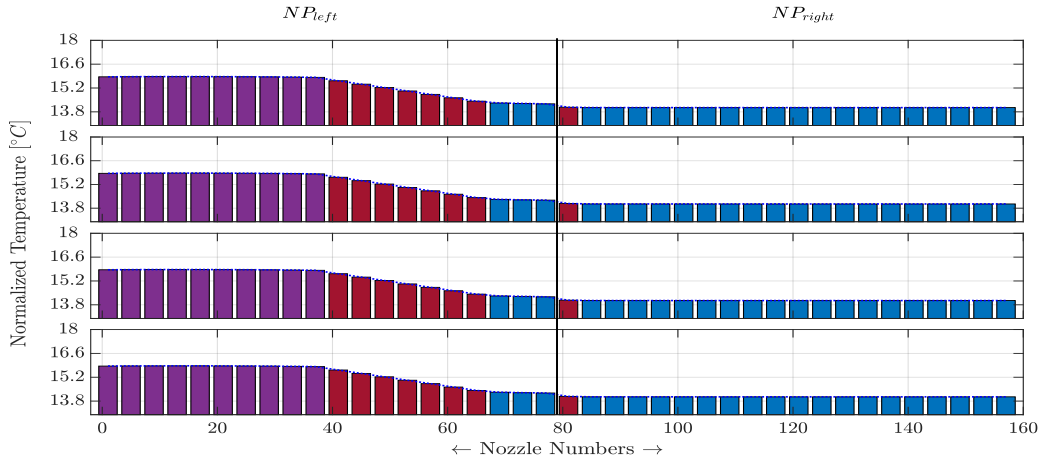

(a) Controlled Scenario: NP_{left} is fully used for jetting. Maximum absolute difference of temperature between two adjacent nozzles is $\mathbf{0.1988}^{\circ}C$.

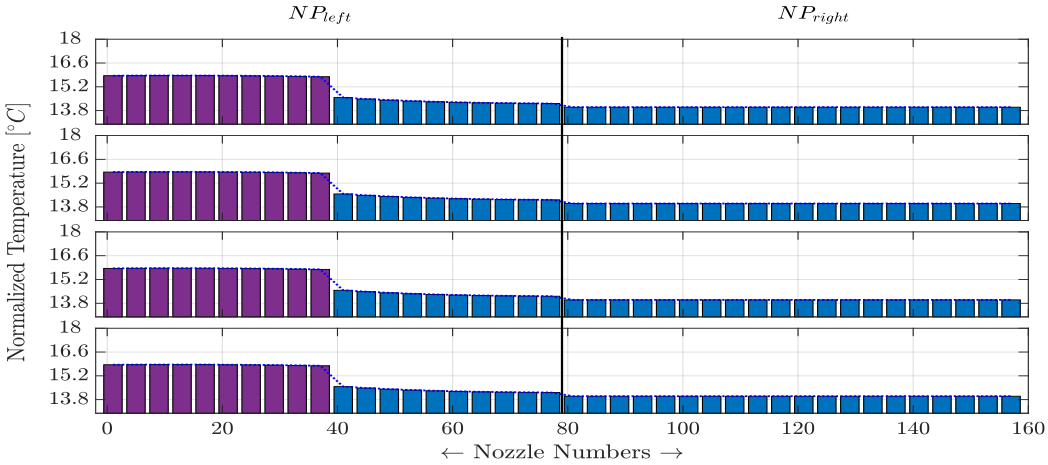

(b) Uncontrolled Scenario: NP_{left} is fully used for jetting. Maximum absolute difference of temperature between two adjacent nozzles is $\mathbf{1.2292}^{\circ}C$.

Fig. 19: Up-scaled controller for 160 nozzles. ■ denotes nozzles that are jetting. ■ denotes the adjacent nozzles that are used as thermal actuators. ■ denotes the nozzles that are not used for heating.

Due to the modularity of the digital twin, up-scaling (or changing) the number of nozzles does not require rebuilding the entire model. The digital twin and the control software are automated to build an up-scaled model with a user-defined number of nozzles, implement in situ sensing-actuation scheme using the bit-map and visualize results of the closed-loop system once the MPC is applied. To demonstrate that, the same printhead, shown in figure 1a, is equipped with 160 nozzles that are equally divided over NP_{left} and NP_{right}. In each side, there are 80 nozzles that are equally distributed over four rows. In figure 19, the result of MPC applied configuration is shown when half the nozzles in NP_{left} are used for jetting.

Remark VI.1. (On computational complexity) With an increasing number of the nozzles, evidently, the computational complexity of solving MPC increases. At a specific iteration of k, the number of decision variables is related to the number of states, the number of control inputs and the number of horizons. Let these numbers be n_x , n_h^k and N respectively. In contrast to solving (21)-(22) that has a complexity of $\mathcal{O}(N^3(n_x + n_h^k)^3)$, the dense LCQP (23) has a lower complexity $\mathcal{O}(N^3{n_h^k}^3)$ [23]. This is achieved by eliminating the states from the decision variables with substitution of equality constraints. However, in this more condensed formulation, the sparsity of matrices is partially lost [25]. Yet the dense LCQP (23) is to be preferred from a computational point of view as the dimension of decision variables involves only the number of non-jetting heating actuators. This is typically small in number.

VII. CONCLUDING REMARKS

In this paper, a modular and flexible digital twin is presented for modeling and control of thermo-fluidic processes in a DoD inkjet printhead. In particular, no additional sensors or actuators are incorporated by developing an in situ sensing-actuation based control strategy that minimizes the liquid temperature fluctuations among individual nozzle. To this end, an experimentally validated graph-theoretic modeling framework is developed that is modular up to an arbitrary number of

Preprints (www.preprints.org) | NOT PEER-REVIEWED | Posted: 22 April 2020 doi:10.20944/preprints202003.0355.v2

nozzles. It is demonstrated that this model is flexible, scalable and versatile and that a number of equivalent input-state-output representations can be derived in a straightforward and explicit manner from the model, depending on the intended application.

A control strategy is implemented without using additional sensors and without using additional actuators. Specifically, to circumvent this limitation, the piezoelectric elements at every individual nozzle serves three roles: a) it is a jetting actuator for depositing liquid, b) it is a soft sensor for estimating liquid temperature, and c) it is a control actuator to diminish gradient in liquid temperature among nozzles. Once a voltage pulse is applied to a piezoelectric material, the soft sensor uses its self-sensing mechanism to measure the acoustic signal. An algorithm is presented that uses the energy of this acoustic signal to estimate the liquid temperature at every individual nozzle. An MPC controller is developed to maintain the fluctuation of liquid temperature among nozzles well below a range of $\pm 0.3^{\circ}$C while using only non-jetting piezoelectric elements as thermal actuators.

The trade-off studies related to different control architectures, e.g. decentralized or distributed architectures for reducing signal overload and faster MPC computation are not addressed in this paper. Moreover, designing and scheduling non-jetting voltage pulses that are required to apply control input without forming droplets of liquid are not discussed in this paper.

References

[1] S. W. Crompton, "The printing press. transforming power of technology," vol. 1, p. 125, 2004.

[2] M. G. Wassink, "Inkjet printhead performance enhancement by feedforward input design based on two-port modeling," Ph.D. dissertation, Technische Universiteit Delft, Netherlands, February 2006.

[3] C. H. Séquin, "Rapid prototyping: A 3D visualization tool takes on sculpture and mathematical forms," *Communications in ACM*, vol. 48, no. 6, pp. 66–73, Jun. 2005.

[4] A. Khalate, "Model-based feedforward control for inkjet printheads," Ph.D. dissertation, Technische Universiteit Delft, Netherlands, December 2013.

[5] XAAR. Product Description. https://www.xaar.com/en/products/xaar-printheads/xaar-1003-c/. [Online; accessed 17-Mar-2020].

[6] A. Khalate, X. Bombois, S. Ye, R. Babuka, and S. Koekebakker, "Minimization of cross-talk in a piezo inkjet printhead based on system identification and feedforward control," *Journal of Micromechanics and Microengineering*, vol. 22, no. 11, 2012.

[7] W. Zapka, *Handbook of Industrial Inkjet Printing: A Full System Approach*. Wiley-VCH Verlag gmbH & Company, 2018, vol. 2.

[8] D. B. Bogy and F. E. Talke, "Experimental and theoretical study of wave propagation phenomena in drop-on-demand ink jet devices," *IBM J. Res. Dev.*, vol. 28, no. 3, pp. 314–321, May 1984.

[9] H. Wijshoff, "Structure and fluid dynamics in piezo inkjet printheads," Ph.D. dissertation, Technische Universiteit Delft, January 2008.

[10] S. Koekebakker, M. Ezzeldin, A. Khalate, R. Babuška, X. Bombois, P. van den Bosch, G. Scorletti, S. Weiland, H. Wijshoff, R. Waarsing, and W. de Zeeuw, *Piezo Printhead Control: Jetting Any Drop at Any Time*. New York, NY: Springer New York, 2013, pp. 41–85.

[11] J. H. Lienhard IV and J. H. Lienhard V, "A heat transfer textbook, fourth edition," *Phlogiston Press*, 2017.

[12] K. J. Kircher and K. M. Zhang, "On the lumped capacitance approximation accuracy in RC network building models," *Energy and Buildings*, vol. 108, pp. 454–462, 2015.

[13] D. Yi and M. Zhang, "Heat flux investigations during flame thermal spray process using the lumped capacitance method," *Applied Thermal Engineering*, 2017.

[14] U. Muschelknautz, *VDI Heat Atlas*. Springer Berlin Heidelberg, 2010.

[15] A. A. Khalate, X. Bombois, G. Scorletti, R. Babuska, S. Koekebakker, and W. de Zeeuw, "A waveform design method for a piezo inkjet printhead based on robust feedforward control," *Journal of Microelectromechanical Systems*, vol. 21, no. 6, pp. 1365–1374, 2012.

[16] R. Ambur and S. Rinderknecht, "Self-sensing techniques of piezoelectric actuators in detecting unbalance faults in a rotating machine," *Procedia Engineering*, vol. 144, pp. 833 – 840, 2016, international Conference on Vibration Problems 2015.

[17] K. Kwon, "Waveform design methods for piezo inkjet dispensers based on measured meniscus motion," *Journal of Microelectromechanical Systems*, vol. 18, no. 5, pp. 1118–1125, Oct 2009.

[18] A. van der Bos, R. Jeurissen, M. Versluis, D. Lohse, H. Reinten, H. Wijshoff, M. van den Berg, and J. de Jong, "Acoustic measurement of bubble size and position in an ink jet printhead." *The Journal of the Acoustical Society of America*, 2013.

[19] H. Usuda, "Droplet discharging apparatus and method," 2004, patent no. US2004/0135832A1. [Online]. Available: http://www.freepatentsonline.com/y2004/0135832.html

[20] H. Nishimura, "Temperature uniformity across an inkjet head using piezoelectric actuation," 2017, patent no. EP3213918A1. [Online]. Available: https://patentimages.storage.googleapis.com/44/e3/87/46409e57a578aa/EP3213918A1.pdf

[21] U. Maeder, F. Borrelli, and M. Morari, "Linear offset-free model predictive control," *Automatica*, vol. 45, no. 10, pp. 2214 – 2222, 2009.

[22] D. Mayne, J. Rawlings, C. Rao, and P. Scokaert, "Constrained model predictive control: Stability and optimality," *Automatica*, vol. 36, no. 6, pp. 789 – 814, 2000.

[23] J. Maciejowski, *Predictive Control with Constraints*. Prentice Hall, 2002.

[24] R. Tóth, M. Lovera, P. S. Heuberger, M. Corno, and P. M. Van den Hof, "On the discretization of linear fractional representations of lpv systems," *IEEE Transactions on Control Systems Technology*, vol. 20, no. 6, pp. 1473–1489, 2012.

[25] J. L. Jerez, E. C. Kerrigan, and G. A. Constantinides, "A sparse and condensed qp formulation for predictive control of lti systems," *Automatica*, vol. 48, no. 5, pp. 999 – 1002, 2012.